

## 2D/2D HETEROSTRUCTURE OF FLOWER-LIKE MoS<sub>2</sub> NANOSPHERES ANCHORED ON g-C<sub>3</sub>N<sub>4</sub> NANOSHEETS FOR REDUCING FRICTION AND WEAR

M.Q. XUE<sup>a</sup>, G.H. NI<sup>a</sup>, A.X. PAN<sup>a</sup>, J. XU<sup>b\*</sup>

<sup>a</sup>*Changzhou Institute of Industry Technology, Changzhou, Jiangsu 213164, P. R. China*

<sup>b</sup>*School of physics and electrical engineering, School of Materials Science and Engineering, Jiangsu University, Zhenjiang, Jiangsu province 212013, P. R. China*

Novel 2D/2D structural nanocomposites of g-C<sub>3</sub>N<sub>4</sub>/MoS<sub>2</sub> with high tribological properties was fabricated through a facile one-step process. The tribological properties of the as-prepared g-C<sub>3</sub>N<sub>4</sub>/MoS<sub>2</sub> as additives in the HVI500 base oil are evaluated by an UMT-2 multi-specimen tribo-tester and the topography of worn scars was obtained using a common SEM, which indicates the minimal friction coefficient (~0.10) and wear rate ( $3.86 \times 10^{-5}$  mm<sup>3</sup>/Nm) and demonstrate the accentuating improvement in reducing-friction and anti-wear properties. The enhanced tribological performance of base oil can be ascribed to the combination of g-C<sub>3</sub>N<sub>4</sub> and spherical-like MoS<sub>2</sub> to share the role of synergistic lubrication. More importantly, our work provides a fresh insight into designing lubricating oil additive and extending the 2D/2D structural nanocomposites.

(Received August 16, 2020; Accepted February 23, 2021)

*Keywords:* MoS<sub>2</sub>, g-C<sub>3</sub>N<sub>4</sub>, Nanocomposites, Liquid paraffin, Tribological properties

### 1. Introduction

As we know, with the development of economy, the problems of energy shortage and environmental pollution bring challenge to sustainable development of our nation economy [1-3]. Studies showed that major variables impacting fuel economy are friction loss [4-7]. If we can reduce the friction consumption which are useless energy savings can be substantial. With the development of nanotechnology in recent years, researchers are increasingly exploring the lubricating oil by adding nano-materials, and the quality of lubricating oil depends on the level of additive and materials [8-12].

Due to their unique structure and excellent properties, two-dimensional (2D) layered nanomaterials have triggered considerable interest in the fields of physics, chemistry and material science [13-17]. The most typical case is graphene, and it is a flat sheet of carbon just one atom thick—with the carbon atoms arranged in a honeycomb lattice [18-22]. Another typical two-dimensional material is molybdenum disulfide (2H-MoS<sub>2</sub>), and the sandwich interlayer

---

\* Corresponding author: xjing@ujs.edu.cn  
<https://doi.org/10.15251/CL.2021.182.91>

structure formed by the stacking of the S–M–S layers, which are loosely bound to each other only by van der Waals forces and are easily cleaved [23-27]. As a lubricant, MoS<sub>2</sub> nanomaterials exhibit low friction coefficients and have a long lifetime in dry air, inert or vacuum environments. However, the unstable dispersibility and serious aggregation of MoS<sub>2</sub> nanostructures largely restrain its actual applications, resulting in unstable tribological properties. However, carbon nitride which comprises physical and chemical properties, and the g-C<sub>3</sub>N<sub>4</sub> boasts extraordinary stability under high temperature and lubricating performance [28-30]. Can the combination of two kinds of materials give play to their respective advantages? Xu prepared MoS<sub>2</sub>/WS<sub>2</sub> nanometer heterojunctions with excellent performance by the solid phase reaction, which exhibits good friction stability and good load resistance [31]. Therefore, the idea of constructing 2D/2D nanocomposite based on 2D structure of MoS<sub>2</sub> was proposed, and the synergistic effect of the two was utilized to give it more excellent tribological properties than a single component.

In this chapter, 2D/2D structural nanocomposites of g-C<sub>3</sub>N<sub>4</sub>/MoS<sub>2</sub> was conducted based on the soft and inexpensive g-C<sub>3</sub>N<sub>4</sub> and environmentally friendly, and the abundant functional groups on its surface enabled MoS<sub>2</sub> to grow in situ on the surface of g-C<sub>3</sub>N<sub>4</sub> nanosheet. The hybrid composite of g-C<sub>3</sub>N<sub>4</sub> and MoS<sub>2</sub> nanosheet can result in lattice mismatch and reduced the interlaminar shear strength of the two kinds of 2D materials, which can improve their tribological properties. In addition, the friction properties of nanocomposites of g-C<sub>3</sub>N<sub>4</sub>/MoS<sub>2</sub> are also investigated from the interface structure, interface effect and friction mechanism of the structure-activity relationship and synergy.

## **2. Experimental section**

### **2.1. Synthesis of 2D g-C<sub>3</sub>N<sub>4</sub> and g-C<sub>3</sub>N<sub>4</sub>/MoS<sub>2</sub>**

The melamine urea were introduced into 25 ml alumina crucible with a cover, and then transferred to the muffle furnace by heating from room temperature to 550°C at a ramp rate of 20 °C/min for 4h. After being cooled down to room temperature, the yellow powder of g-C<sub>3</sub>N<sub>4</sub> was collected and ground into powder.

Take the preparation of g-C<sub>3</sub>N<sub>4</sub> (0.15g) dispersed in 60 ml of deionized water to obtain a well-dispersed suspension by ultrasonication for 1 h. Then (NH<sub>4</sub>)<sub>6</sub>Mo<sub>7</sub>O<sub>24</sub>·4H<sub>2</sub>O (0.6617g), HONH<sub>3</sub>Cl (0.5730 g) and CH<sub>4</sub>N<sub>2</sub>S (0.5707g) were added to the dispersion with a magnetic stirrer for an hour, then the mixture was transferred into an autoclave (75% in volume) by heating at 190 °C for 24 h. The resulting precipitate was washed with distilled water several times and then centrifuged with ethanol. Finally, the product was dried in a vacuum oven at 60°C for 12 h, thereby gaining g-C<sub>3</sub>N<sub>4</sub>/MoS<sub>2</sub> nanocomposites. The preparation route of g-C<sub>3</sub>N<sub>4</sub>/MoS<sub>2</sub> nanocomposites is shown in Fig. 1.

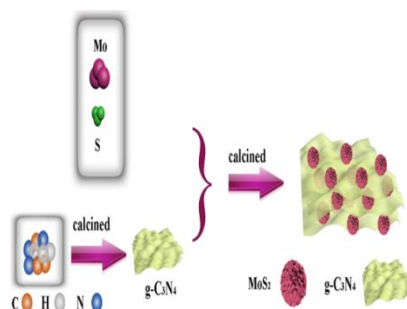


Fig. 1. The preparation route of  $g\text{-C}_3\text{N}_4/\text{MoS}_2$  nanocomposite.

## 2.2. Characterization

XRD analysis via Bruker-AXS, Germany, FT-IR spectra via Thermo Nicolet Model Nexus 470, USA and Raman via DXR-Thermo Scientific, USA were performed to analyze phase structure and chemical composition of the as-prepared nanomaterials. SEM via JEOL JXA-840A, Japan and TEM via JEM-100CX II, Japan were performed to examine the surface micromorphology and structure.

## 2.3. Tribological test

In this work, a multispecimen friction and wear tester (MS-T3001, China) with ball-on-disk construction was used to evaluate the tribological properties of the oil mixtures contained with nano-additives. And liquid paraffin was used as the lubricating oil in the friction experiments. During experiments, the rotary velocity of the steel ball was kept 200 rpm, and the applied load was set to 2 N for 0.5 h at room temperature. Also, different tribological variables including the additive concentration (0.7-7w%), rotary velocity (100-500 rpm), and applied load (2-6 N) were investigated. More importantly, all friction experiments were investigated three times, respectively. After that, the surface topography of the wear scar was analyzed by scanning electron microscope (SEM, HITACHI S-3400N, Japan) and non-contact optical 3D profilers (SMP, NT1100, Veeco WYKO, USA).

## 3. Results and discussion

The crystal phase and crystal structures of  $g\text{-C}_3\text{N}_4$ ,  $\text{MoS}_2$ ,  $g\text{-C}_3\text{N}_4/\text{MoS}_2$  were examined by X-ray diffraction (XRD). Fig. 2a presents the XRD patterns of all the composite samples. The pristine  $g\text{-C}_3\text{N}_4$  had a strong peak located at  $2\theta$  of  $27.4^\circ$  and the weak peak at  $13.1^\circ$  correspond to the (002) and (100) planes of  $g\text{-C}_3\text{N}_4$  (JCPDS No.87-1526), respectively [32-35]. The diffraction peaks of  $\text{MoS}_2$  are indexed to the (002), (100), (103), and (110) peaks of 2H- $\text{MoS}_2$  (JCPDS No.37-1492,  $a=3.161 \text{ \AA}$ ,  $c=12.299 \text{ \AA}$ ) [36-38]. For  $g\text{-C}_3\text{N}_4/\text{MoS}_2$  composites, the main characteristics of diffraction peak for  $\text{MoS}_2$  and  $g\text{-C}_3\text{N}_4$  were visible in the XRD pattern. However, the weak diffraction peak of  $g\text{-C}_3\text{N}_4$  is detected, due to the low content of  $g\text{-C}_3\text{N}_4$  in the sample and the  $\text{MoS}_2$  attached to the surface of the  $g\text{-C}_3\text{N}_4$ , which hindered the agglomeration of  $g\text{-C}_3\text{N}_4$  nanosheet. Meanwhile, the  $\text{MoS}_2$  diffraction peak intensity were decreased for the addition of  $g\text{-C}_3\text{N}_4$ , especially (002) peak. From the selected areas of the Fig. 2b, the peak intensity of (002) gradually reduced with the increase of content of  $g\text{-C}_3\text{N}_4$  gradually, and shifted toward low diffraction angle. This suggests that introduction of  $g\text{-C}_3\text{N}_4$  can effectively inhibit the growth of  $\text{MoS}_2$  crystal in composite materials and effectively avoid the agglomeration of  $\text{MoS}_2$  nanosheet, therefore the nanosheet with thinner and smaller size structure were obtained.

The FTIR spectra of  $g\text{-C}_3\text{N}_4$ ,  $\text{MoS}_2$ , and  $g\text{-C}_3\text{N}_4/\text{MoS}_2$  were shown in Fig. 2c. For the pristine  $\text{MoS}_2$ , the characteristic peaks at  $593 \text{ cm}^{-1}$  can be observed, corresponding to vibrational modes of Mo-S. The peak profile of the  $g\text{-C}_3\text{N}_4/\text{MoS}_2$  is similar to that of the  $g\text{-C}_3\text{N}_4$ , which suggests that the introduction of  $\text{MoS}_2$  don't change the functional groups of  $g\text{-C}_3\text{N}_4$ . Characteristic peaks from  $g\text{-C}_3\text{N}_4/\text{MoS}_2$  were clearly observed at  $809 \text{ cm}^{-1}$  and  $1243\text{-}1636 \text{ cm}^{-1}$ , which can be attributed to the C-H out-of-plane bending vibration of the 1,4-disubstituted rings

and the stretching vibrations of  $\gamma(\text{C-NH-C})$ ,  $\gamma(\text{C=N})$ , respectively. The broadband in the range of  $3000\text{-}3500\text{ cm}^{-1}$  show N-H and O-H stretching vibration modes. Importantly, an reduce on peak intensity in the spectrum of the  $\text{g-C}_3\text{N}_4/\text{MoS}_2$  in comparison with the  $\text{g-C}_3\text{N}_4$ , which indicate that the effect of heterojunctions between  $\text{g-C}_3\text{N}_4$  and  $\text{MoS}_2$  weaken the vibration of the g-groups for  $\text{g-C}_3\text{N}_4$  and the nano heterojunction of  $\text{g-C}_3\text{N}_4/\text{MoS}_2$  be successfully synthesized.

Fig. 2d shows the Raman spectroscopy of the prepared  $\text{MoS}_2$  and  $\text{g-C}_3\text{N}_4/\text{MoS}_2$ . Two strong Raman peaks of  $\text{MoS}_2$  are detected at  $377$  and  $403\text{ cm}^{-1}$ , corresponding to the  $\text{E}_{2g}^1$  and  $\text{A}_{1g}$  phonon vibration modes of  $\text{MoS}_2$ . In addition, the same characteristic peaks were found for  $\text{g-C}_3\text{N}_4/\text{MoS}_2$ . It is worth noting that a slight red shift with the peak of  $\text{A}_{1g}$  and a slight blue shift with the peak of  $\text{E}_{2g}^1$  are existence in Fig.2e [39-40]. The frequency difference of  $\text{g-C}_3\text{N}_4/\text{MoS}_2$  significantly is smaller than the pure  $\text{MoS}_2$ , which suggests that the introduction of  $\text{g-C}_3\text{N}_4$  inhibits the growth of  $\text{MoS}_2$  crystal to gain the thinner nanosheets of  $\text{MoS}_2$ . Therefore, spectroscopy technologies including Raman, X-ray diffraction (XRD) and fourier transform infrared spectroscopy (FTIR) were employed to further confirm the successful synthesis of  $\text{g-C}_3\text{N}_4/\text{MoS}_2$  and their quality.

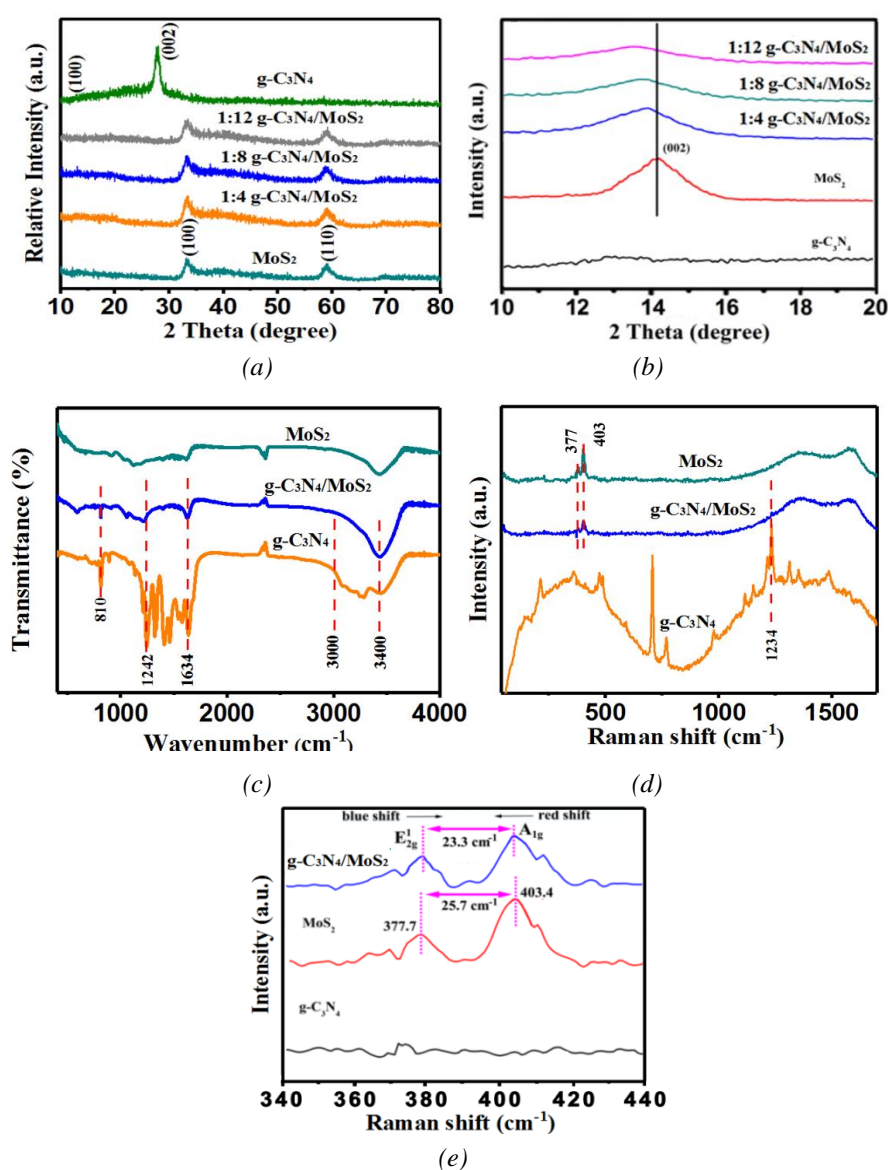


Fig. 2. (a) XRD patterns of pure  $\text{g-C}_3\text{N}_4$ , pure  $\text{MoS}_2$  and  $\text{g-C}_3\text{N}_4/\text{MoS}_2$  nanocomposite; (b) High magnification XRD patterns of pure  $\text{MoS}_2$  and  $\text{g-C}_3\text{N}_4/\text{MoS}_2$  of the selected area in Fig. 2a; FTIR (c) and Raman (d) pure  $\text{g-C}_3\text{N}_4$ , pure  $\text{MoS}_2$  and  $\text{g-C}_3\text{N}_4/\text{MoS}_2$  nanocomposite, (e) the magnified pattern of the selected area in (d).

The morphologies and microstructures of the  $g\text{-C}_3\text{N}_4$ ,  $\text{MoS}_2$  and  $g\text{-C}_3\text{N}_4/\text{MoS}_2$  were further characterized by SEM and TEM. As can be seen from Fig. 3 a, the prepared  $g\text{-C}_3\text{N}_4$  is of irregular structure similar to graphene with sizes larger than 100 nm. In Fig. 3b, sphere-like structure are observed for  $\text{MoS}_2$ . Interestingly, the  $\text{MoS}_2$  nanosheets could form nanoflakes and then nanoflakes aggregate to form the loose sphere-like architectures. Fig. 3c and Fig. 3d is a representative SEM image of the  $g\text{-C}_3\text{N}_4/\text{MoS}_2$ . As seen in Fig. 3d, the self-assembled globular structure of  $\text{MoS}_2$  disappeared, more loosely, uniform and fine nanosheets structure appeared with no agglomeration. TEM (Fig. 3e) image could demonstrate the detailed microstructure, and it can be clearly seen that most of the  $\text{MoS}_2$  flower-like sheets uniformly were formed on the surface of the  $g\text{-C}_3\text{N}_4$ , which indicates that the  $g\text{-C}_3\text{N}_4$  sheets provide favorable sites for the growth of the  $\text{MoS}_2$ , and the  $g\text{-C}_3\text{N}_4/\text{MoS}_2$  consists of few-layered  $g\text{-C}_3\text{N}_4$  sheets and well-crystallized  $\text{MoS}_2$  nanosheets that are strongly bonded with the  $g\text{-C}_3\text{N}_4$  sheets. Furthermore, the Fig.3f exhibits the ultrathin curved nanosheets with an average lattice spacing of 0.95 nm, which is closer to (100) plane of 2H- $\text{MoS}_2$ , and  $\text{MoS}_2$  nanosheet became smaller and more uniform, compared with pure  $\text{MoS}_2$ . Hence, a moderate amount of  $g\text{-C}_3\text{N}_4$  may prevent the  $\text{MoS}_2$  nanoparticles aggregating and form perfect 2D nano-heterojunction.

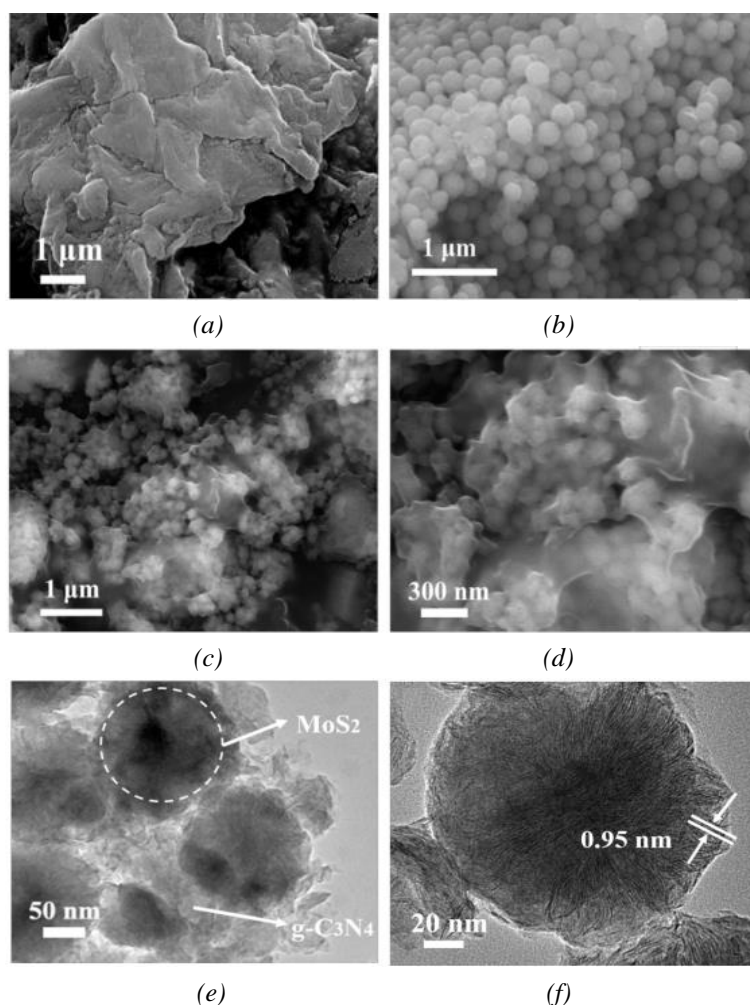


Fig. 3. SEM images of (a)  $g\text{-C}_3\text{N}_4$ , (b)  $\text{MoS}_2$ , (c)&(d)  $g\text{-C}_3\text{N}_4/\text{MoS}_2$ ; TEM images of (e)&(f)  $g\text{-C}_3\text{N}_4/\text{MoS}_2$ .

The dispersion and stability of  $g\text{-C}_3\text{N}_4$ ,  $\text{MoS}_2$  and  $g\text{-C}_3\text{N}_4/\text{MoS}_2$  composite in paraffin oil as a function of time is first investigated and depicted in Fig. 4. Clearly, no observable precipitations appeared and the oil mixture can remain stable even after 24 h for  $g\text{-C}_3\text{N}_4/\text{MoS}_2$  composite. However, clear sedimentation appeared in the mixed oil containing  $\text{MoS}_2$  nanospheres after 24 h.



Fig. 4. The dispersion and stability experiments: (a)  $g\text{-C}_3\text{N}_4$ , (b)  $\text{MoS}_2$  and (c)  $g\text{-C}_3\text{N}_4/\text{MoS}_2$  composites in liquid paraffin at the concentration of 3 w%.

In order to evaluate the tribological properties of the  $g\text{-C}_3\text{N}_4/\text{MoS}_2$  nanocomposite as lube oil additives, experiments were conducted by a ball-on-disk tribometer, as represented in Fig. 5. Fig. 5a shows the friction coefficient of friction (COF) of  $g\text{-C}_3\text{N}_4/\text{MoS}_2$  is kept stable about 0.08, and lowest in all oil samples. Fig. 5b shows the friction coefficient of lubricant with 2N load for the base oil and the base oil containing 0.5wt.%, 1wt.%, 3wt.%, 5wt.% and 7wt.%  $g\text{-C}_3\text{N}_4/\text{MoS}_2$  at the speed of 200rpm for 0.5 h. It depicts that the friction effect is the lowest and the most stable when the addition amount of  $g\text{-C}_3\text{N}_4/\text{MoS}_2$  is 1wt.%. In order to further analyze the friction performance of  $g\text{-C}_3\text{N}_4/\text{MoS}_2$  composite, the experiments was investigated by two different situations of load and speed.

Fig. 5c directs the friction coefficient of the pure base oil, 2.0 wt.% of  $g\text{-C}_3\text{N}_4$ , 2.0 wt.% of  $\text{MoS}_2$  and 2.0 wt.% of  $g\text{-C}_3\text{N}_4/\text{MoS}_2$  increasing with the load increases, and the liquid paraffin containing  $g\text{-C}_3\text{N}_4/\text{MoS}_2$  composites exhibit remarkably low and stable COF. Meanwhile, the lowest COF (0.08) was observed at an applied load of 5 N in the case of  $g\text{-C}_3\text{N}_4/\text{MoS}_2$  composites. Interestingly, the curves of COF vs rotating speeds display similar behavior as represented by COF curves against applied loads (Fig. 5d), which also indicate the positive influence of rotating speeds friction behaviors is mainly attributable to the addition and synergistic effect of  $g\text{-C}_3\text{N}_4$  and  $\text{MoS}_2$  in composite systems.

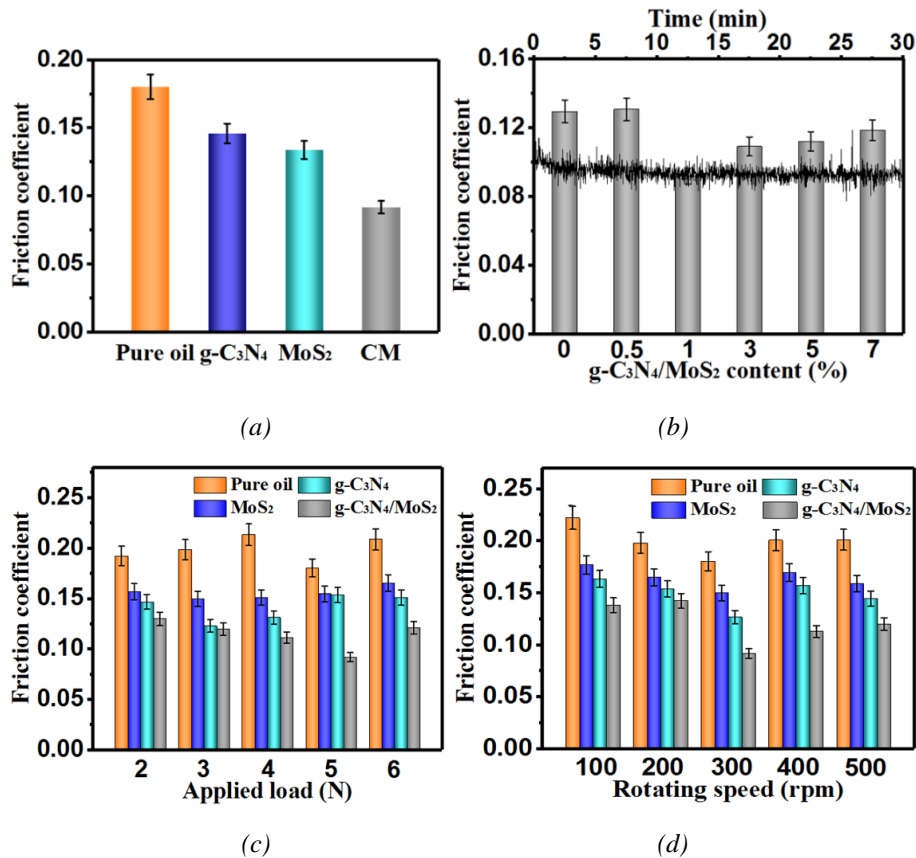


Fig. 5. (a) Friction coefficient of liquid paraffin contained with various oil additive; (b) Friction coefficient of liquid paraffin contained with different g-C<sub>3</sub>N<sub>4</sub>/MoS<sub>2</sub> composites additive; Variations of mean friction coefficient of paraffin with different additive (c) increasing load (2-6 N), (d) under diverse speeds (100-500 rpm).

For further explore the wear resistance tribological properties of the g-C<sub>3</sub>N<sub>4</sub>/MoS<sub>2</sub> composites, the topography of the worn scar was examined by SEM. Fig. 6 shows the wear scar diagram of the base oil with different additive contents, Fig. 6a is the wear scar diagram of pure base oil, it can be seen that the wear scar is very rough, with a large number of deep furrows appearing and a small amount of sticking occurring, which indicates that the direct contact of the friction pairs is resulted from the damage of the pure base oil film under high load. Conversely, the worn surfaces of mixed oil containing g-C<sub>3</sub>N<sub>4</sub>, MoS<sub>2</sub>, and g-C<sub>3</sub>N<sub>4</sub>/MoS<sub>2</sub> composite retain slight trace, their wear scar is much shallower and narrower than that of pure paraffin (Fig. 6b-6d). As shown in the Fig. 6d, the surface lubricated with g-C<sub>3</sub>N<sub>4</sub>/MoS<sub>2</sub> only presents slender furrows and the friction performance is the best. Furthermore, SMP analysis presented accurate 3D images of the wear scar of steel disk, and resulted in Fig. 7. For liquid paraffin, the wear scar width and depth are approximately 262 μm and 7.2 μm, respectively, as shown Fig. 7a. Similarly, the SMP analysis of paraffin oil contained with g-C<sub>3</sub>N<sub>4</sub>, MoS<sub>2</sub>, and g-C<sub>3</sub>N<sub>4</sub>/MoS<sub>2</sub> composite have the same results of SEM (Fig. 7b-7d). While for g-C<sub>3</sub>N<sub>4</sub>/MoS<sub>2</sub> composite using as an additive of paraffin oil, the wear scar width and depth were appreciably decreased, and their values are about 220 μm and 0.81 μm (Fig. 7d), which is also in agreement with SEM results of wear scar. Additionally, all the above

friction and wear results revealed  $g-C_3N_4/MoS_2$  composite as the oil additives possess superior friction-reduction and anti-wear.

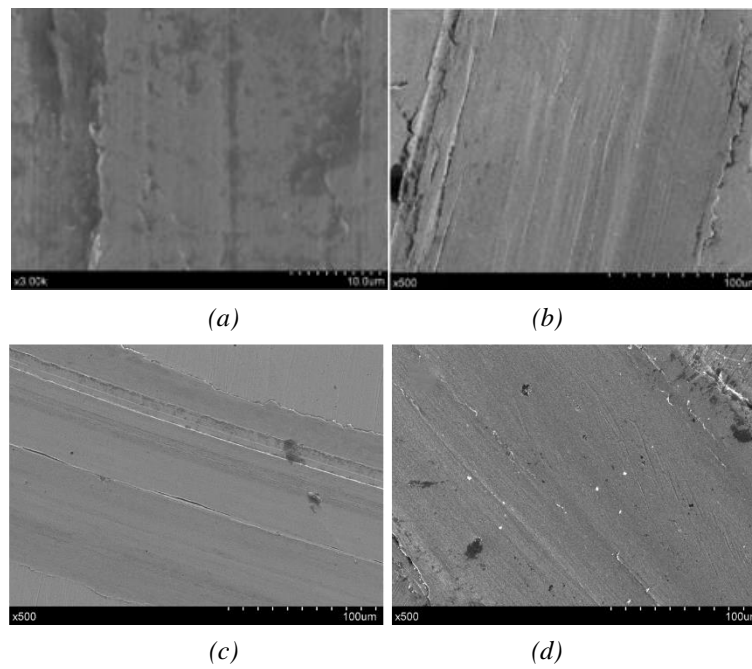


Fig. 6. SEM images of worn surfaces of (a) liquid paraffin, and liquid paraffin contained with (b)  $g-C_3N_4$ ; (c)  $MoS_2$  and (d)  $g-C_3N_4/MoS_2$  composites.

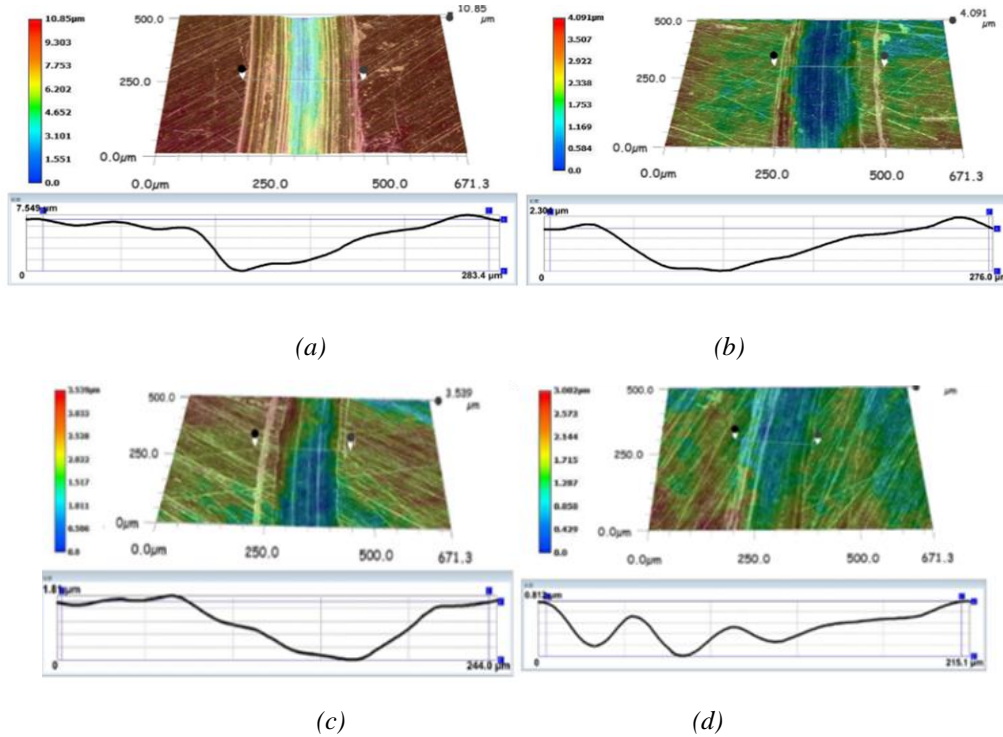


Fig. 7. Noncontact three-dimensional images of worn surfaces of (a) liquid paraffin; and liquid paraffin contained with (b)  $g-C_3N_4$ ; (c)  $MoS_2$  and (d)  $g-C_3N_4/MoS_2$  composites.

The surface morphology of wear scar, nanoparticles and its element distribution have been tested and analyzed to describe the tribological mechanism of 2D/2D  $g\text{-C}_3\text{N}_4/\text{MoS}_2$  nanostructures by SEM and EDS. Fig. 8a shows that many wear debris and deep furrows with delaminated layers were observed on the surface of steel disc lubricated with pure paraffin. After adding  $g\text{-C}_3\text{N}_4/\text{MoS}_2$  in liquid paraffin (Fig. 8b), several slender damages or wear appeared on the surface, and the continuous black lubricating film forms gradually on the sample surface with the friction process, hence the friction coefficient and wear loss increased. The observed composition of wear scar by EDS analysis (Fig. 8c and 8d), the appearance of C, N, Mo, and S elements on the wear surface also reveals  $g\text{-C}_3\text{N}_4/\text{MoS}_2$  nanocomposite could be transferred to the friction contact region and formed the tribo-film during the friction experiment.

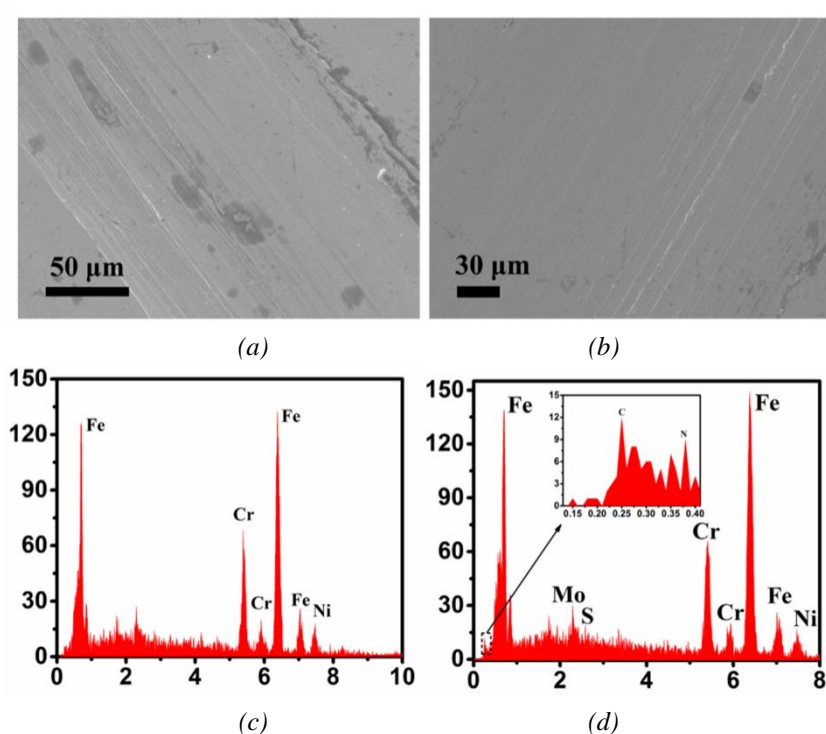


Fig. 8. SEM images and EDS of worn surfaces of (a, c) liquid paraffin and (b, d)  $g\text{-C}_3\text{N}_4/\text{MoS}_2$  composites.

It can be seen from the above analysis that  $g\text{-C}_3\text{N}_4/\text{MoS}_2$  nanocomposites as the base oil additives can effectively reduce the friction coefficient and improve the load capacity, and the tribological mechanism was proposed and illustrated in Fig. 9. Firstly, Layered structures of  $\text{MoS}_2$  nanoplates could be transferred to the exfoliated phases with fewer layers attributed to the weak Vander Waals interaction between S-S layers for transverse shear effects, and the nanosheets will penetrate more easily into the interface with the base oil, and these nanosheets could strongly adhere to substrates and form continuous film in concave of rubbing surface to avoid direct contact with the friction pair, enhancing the tribological properties. More importantly, a transfer film of  $g\text{-C}_3\text{N}_4/\text{MoS}_2$  in the friction boundary has taken place continuously during the friction process, which not only supports the enhancement in carrying load but also protect the contact surfaces from wearing, and hence lower COFs and excellent antiwear ability have resulted. Therefore, the

enhanced tribological properties of g-C<sub>3</sub>N<sub>4</sub>/MoS<sub>2</sub> nanocomposites can be largely ascribed to the synergistic effect of MoS<sub>2</sub> and g-C<sub>3</sub>N<sub>4</sub>. The conclusion on the wear mechanism of the composite by the debris topography analysis is coincident to that of the SEM analysis on the worn surface.

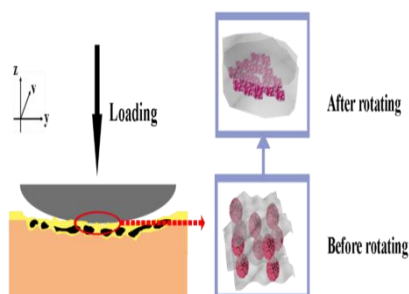


Fig. 9. The tribological mechanism of g-C<sub>3</sub>N<sub>4</sub>/MoS<sub>2</sub> additive in liquid paraffin.

#### 4. Conclusions

In summary, the novel 2D/2D structural nanocomposites of g-C<sub>3</sub>N<sub>4</sub>/MoS<sub>2</sub> have been synthesized by one-step hydrothermal method, which exhibited outstanding reducing-friction and anti-wear performance compared with those of both the bare MoS<sub>2</sub> and the g-C<sub>3</sub>N<sub>4</sub> as a promising lubrication additive for improving the tribological properties of paraffin oil. The improved tribological properties of g-C<sub>3</sub>N<sub>4</sub>/MoS<sub>2</sub> heterostructure was attributed to the intimate interfacial interaction between the g-C<sub>3</sub>N<sub>4</sub> and MoS<sub>2</sub>, which can be summarized as follows: (1) the morphology of the MoS<sub>2</sub> is changed due to the confinement effect of g-C<sub>3</sub>N<sub>4</sub>, and a moderate amounts of g-C<sub>3</sub>N<sub>4</sub> may prevent the MoS<sub>2</sub> nanoparticles aggregating and form perfect 2D nano-heterojunction with a larger surface area, (2) most of the MoS<sub>2</sub> flower-like sheets uniformly were formed on the surface of the g-C<sub>3</sub>N<sub>4</sub> providing favourable sites for the growth of the MoS<sub>2</sub>.

Furthermore, an underlying tribological mechanism of the g-C<sub>3</sub>N<sub>4</sub>/MoS<sub>2</sub>-Oil system was also proposed based on the results of friction experiments and wear scar, which also suggests the enhanced tribological properties are attributed to uniform dispersion, the formation of tribofilm and synergistic effect of g-C<sub>3</sub>N<sub>4</sub>/MoS<sub>2</sub> heterojunction.

#### Acknowledgments

This work was funded by Natural Science Foundation of Jiangsu Province (BK20201424), Changzhou Sci&Tech Program (grant no. CJ20190017) and the Key Program for Research Team of Changzhou Institute of Industry Technology (grant no. ZD 201813101003).

## References

- [1] L. Chen, Y.-Z. Sun, L. Li, Y.-P. Ren, X.-D. Ren, *Appl. Surf. Sci.* **518**, 145981 (2020).
- [2] L.-Y. Zhang, C.-T. Peng, J. Shi, Y.-X. Jin, Y.-X. R.-F. Lu, *J. Alloys Compd.* **828**, 154460 (2020).
- [3] K.-Y. Wang, R. He, J.-H. Tang, R.-C. Liu, *2020 Therm. Sci.* **24**, 1827 (2020).
- [4] C.-Y. Min, Z.-B. He, H.-Y. Liang, D.-D. Liu, C.-K. Dong, H.-J. Song, Y.-D. Huang, *Polym. Compos.* **41**, 1624 (2020).
- [5] Y.-H. Zhang, Y.-H. Fu, X.-J. Hua, L. Quan, J.-J. Qu, *Wear* **448**, 203216 (2020).
- [6] H.-Y. Liang, Y.-F. Bu, Y.-H. Zhang, X.-J. Xu, J.-Y. Zhang, *Mater. Lett.* **233**, 310 (2018).
- [7] B.-B. Chen, X. Li, Y.-H. Jia, L. Xu, H.-Y. Liang, X.-F. Li, J. Yang, C.-S. Li, F.-Y. Yan, *Compos. Part A: Appl. Sci. Manufac.* **115**, 157 (2018).
- [8] C.-Y. Min, Z.-B. He, H.-J. Song, D.-D. Liu, W. Jia, J.-M. Qian, Y.-H. Jin, L. Guo, *Appl. Sci.* **9**, 170 (2019).
- [9] L.-L. Tang, N. Wang, Z.-Y. Han, H.-H. Sun, D.-S. Xiong, *Colloid Surface A* **594**, 124655 (2020).
- [10] Z.-P. Wang, L. Qian, Z.-X. Jiang, X. Xue, K. Reddy, *AIP Adv.* **10**, 045013 (2020).
- [11] J. Yang, B.-B. Chen, H.-J. Song, H. Tang, C.-S. Li, *Cryst. Res. Technol.* **49**, 926 (2014).
- [12] J. Yang, H.-T. Zhang, B.-B. Chen, H. Tang, C.-S. Lia, Z.-Z. Zhang, *RSC Adv.* **5**, 64254 (2015).
- [13] M.-S. Zhang, B.-B. Chen, H. Tang, G.-G. Tang, C.-S. Li, L. Chen, H.-M. Zhang, Q. Zhang, *RSC Adv.* **5**, 1417 (2015).
- [14] X. Chen, D.-M. Jiang, H.-Y. Li, K. Xie, Y.-H. Jiang, Y.-Q. Wang, *J. Colloid Interface Sci.* **575**, 168 (2020).
- [15] Y.-P. Chen, Y.-E. Xie, X.-H. Yan, M.-L. Cohen, S.-B. Zhang, *Phys. Rep.* **868**, 1 (2020).
- [16] M.-L. Guan, Q.-W. Wang, X. Zhang, J. Bao, X.-Z. Gong, Y.-W. Liu, *Front. Chem.* **8**, 390 (2020).
- [17] M.-L. Guan, X. Zhang, J. Bao, X.-Z. Gong, *Nanotechnol.* **31**, 085706 (2020).
- [18] R. Xiao, C.-X. Zhao, Z.-Y. Zou, Z.-P. Chen, L. Tian, H.-T. Xu, H. Tang, Q.-Q. Liu, Z.-X. Lin, X.-F. Yang, *Appl. Catal. B-Environ.* **268**, 118382 (2020).
- [19] T. Fei, L.-M. Yu, Z.-Y. Liu, Y.-H. Song, F. Xu, Z. Mo, C.-B. Liu, J.-J. Deng, H.-Y. Ji, M. Cheng, Y.-C. Lei, H. Xu, H.-M. Li, *J. Colloid Interface Sci.* **557**, 498 (2019).
- [20] Y. Liu, J.-Y. Liu, Y.-H. Jiang, M.-J. Meng, L. Ni, H.-L. Qiu, R.-G. Yang, Z.-C. Liu, H.-W. Liu, *Ind. Eng. Chem. Res.* **58**, 22324 (2019).
- [21] C.-Y. Min, Z.-B. He, H.-J. Song, H.-Y. Liang, D.-D. Liu, C.-K. Dong, W. Jia, *Tribol. Int.* **140**, 105867 (2019).
- [22] X.-D. Ren, F.-H. Ma, R.-H. Wang, L. Qian, W.-X. Ma, *AIP Adv.* **9**, 125004 (2019).
- [23] Y.-H. Zhou, Y. Yang, Y.-D. Guo, Q. Wang, X.-H. Yan, *Appl. Surf. Sci.* **497**, 143764 (2019).
- [24] P.-Y. Lin, J. Shen, C. Prasad, H. Tang, Q.-Q. Liu, M.-Y. Zhang, *Ceram. Int.* **45**, 21120 (2019).
- [25] J. Yan, S.-C. Wang, Y. Chen, M. Yuan, Y.-P. Huang, J.-B. Lian, J.-X. Qiu, J. Bao, M. Xie, H. Xu, H.-M. Li, Y. Zhao, *J. Alloys Compd.* **811**, 151915 (2019).
- [26] F.-X. Zhang, X.-Y. Zhang, F.-L. Zhang, G.-G. Tang, C.-S. Li, J. Xu, *Mater. Res. Express.* **6**, 1250 (2019).
- [27] C. Zhou, J.-J. Wang, X.-H. Yan, X.-X. Yuan, D.-F. Wang, Y.-H. Zhu, X.-N. Cheng, *Ceram. Int.*

- 45**, 21534 (2019)
- [28] F.-X. Zhang, G.-G. Tang, J. Xu, C.-S. Li, *Micro Nano Lett.* **14**, 1355 (2019).
- [29] L. Zhu, Y. Wang, F. Hu, H.-J. Song, *Appl. Surf. Sci.* **345**, 349 (2015).
- [30] X.-M. Gao, Y.-L. Fu, D. Jiang, D.-S. Wang, S.-S. Xu, W.-M. Liu, L.-J. Weng, J. Yang, J.-Y. Sun, M. Hu, *Surf. Coat. Tech.* **353**, 8 (2018).
- [31] P.-Y. Lin, J. Shen, H. Tang, Zulfiqar, Z.-X. Lin, Y. Jiang, *J. Alloys Compd.* **810**, 151918 (2019).
- [32] C. Prasad, H. Tang, Q.-Q. Liu, I. Bahadur, S. Karlapudi, Y.-J. Jiang, *Int. J. Hydrog. Energy* **45**, 337 (2020).
- [33] K.-H. Sun, J. Shen, Q.-Q. Liu, H. Tang, M.-Y. Zhang, S. Zulfiqar, C.-S. Lei, *Chinese J. Catal.* **41**, 72 (2020).
- [34] J. Xu, Y.-Y. Xu, G.-G. Tang, H. Tang, H.-B. Jiang, *Appl. Surf. Sci.* **492**, 37 (2019).
- [35] C.-C. Gao, H.-F. Hua, M. Du, J.-S. Liu, X.-Y. Wu, Y. Pu, X.-A. Li, *Appl. Surf. Sci.* **515**, 145842 (2020).
- [36] Y.-X. Han, C. Kong, P.-J. Yan, *Theor. Chem. Acc.* **139**, 98 (2020).
- [37] T.-W. Ouyang, W.-Y. Fan, J.-Q. Guo, Y.-N. Zheng, X.-H. Yin, Y.-L. Shen, *Phys. Chem. Chem. Phys.* **22**, 10305 (2020).
- [38] N. Li, J. Zhou, Z.-Q. Sheng, W. Xiao, *Appl. Surf. Sci.* **430**, 218 (2018).
- [39] Y. Ma, Y.-X. Dong, B. Wang, S.-W. Ren, J.-T. Cao, Y.-M. Liu, *Talanta* **207**, 120288 (2020).
- [40] Y.-Q. He, Z.-Y. Ma, L. Binnah Junior, *Ceram. Int.* **46**, 12364 (2020).